INL/CON-16-40542
PREPRINT

ASSESSMENT OF MULTIPHASE CFD WITH ZERO CLOSURE MODEL FOR BOILING WATER REACTOR FUEL ASSEMBLIES

17th International Topical Meeting on Nuclear Reactor Thermal Hydraulics

Su-Jong Yoon, G. Agostinelli, E. Baglietto

August 2017

The INL is a
U.S. Department of Energy
National Laboratory
operated by
Battelle Energy Alliance

ASSESSMENT OF MULTIPHASE CFD WITH ZERO CLOSURE MODEL FOR BOILING WATER REACTOR FUEL ASSEMBLIES

Su-Jong Yoon
Department of Fusion, Hydrogen & Measurement Sciences
Idaho National Laboratory
2525 Fremont Ave., Idaho Falls, Idaho 83415
sujong.yoon@inl.gov

G. Agostinelli and E. Baglietto
Department of Nuclear Science and Engineering
Massachusetts Institute of Technology
77 Massachusetts Ave., Cambridge, MA 02139
giulia@mit.edu; emiliob@mit.edu

ABSTRACT

Extension of existing boiling closures to the high void fraction conditions of BWRs is one of challenges for M-CFD applications. This paper presents the assessment of an Eulerian M-CFD model with Zero closure that has been specifically designed for two-phase flow and heat transfer applications in BWR fuel assemblies. The baseline Zero closure aims at including the simplest and most robust representation of the key physical mechanisms, rather than aiming at absolute accuracy of the predictions. The capabilities of M-CFD with Zero closure are evaluated against the international OECD/NRC BFBT benchmark data through the comparative analyses of local void fraction, subchannel void fraction error and exit quality. INL high performance computing system has been employed to demonstrate the scalability of the M-CFD application to nuclear reactor fuel assemblies. The M-CFD simulation results show impressive agreement with the experimental data for both quantitative and qualitative results, with the highest uncertainty being observed in the prediction of the local void fraction profile at low void fraction condition. This paper presents a recent view of the best practices for M-CFD of BWR fuel assemblies to provide a useful reference to identify and overcome common challenges in the applications of M-CFD tools. We provide recommendations for geometric modeling, mesh generation and solver configurations to optimize the methodology application.

KEYWORDS
Multiphase CFD, Boiling Water Reactor, BFBT Benchmark, V&V, Best Practice

1. INTRODUCTION

High fidelity Multiphase Computational Fluid Dynamics (M-CFD) modeling is a complex research area that relies on the validity of its mechanistic closures. While extensive effort is being devoted to evaluate and improve the closure validity and predictive capabilities, as part of the Consortium for Advanced Simulation of Light Water Reactors (CASL) effort, the heat and mass transfer characteristics in two-phase flow boiling still remain challenging. For instance, the extension of existing boiling closures to the high void fraction conditions of Boiling Water Reactors (BWR) is still an open issue. The scales that need to be resolved vary widely from the millimeter scale of the multiphase structures to the meters scale of the core geometry. This multi-scale problem requires extremely high computational effort in order to avoid geometric simplifications that would introduce large uncertainty in the computational result. In M-CFD

simulations, which are most commonly based on efficient second order accurate finite volume solution methods, the mesh structure and quality have an observable influence not only on the accuracy of result but also on the robustness of the simulation. While automated unstructured mesh generation, e.g. trimmed mesh, tetrahedral mesh and polyhedral mesh, etc., are desirable from an application viewpoint, control of the mesh quality is not always optimal, or straightforward. Furthermore, the high performance computing capability is a promising solution for M-CFD for nuclear reactor fuel assemblies, but the scalability of parallelization still needs to be assessed and optimized. The physical modeling and computational challenges make CFD simulations of BWR fuel assemblies an important challenge for the industry. Series of studies [1, 2, 3, 4, 5, and 6] have being performed to develop and validate the CFD models for the simulations of two-phase flow phenomena in BWR core. The Eulerian M-CFD model with a baseline 'Zero Closure' has been developed leveraging the experience gained through the Numerical Nuclear Reactor project [3]. In this paper, the Eulerian M-CFD model with Zero Closure is reviewed, and its capabilities for BWR fuel assemblies evaluated against the international OECD/NRC BWR Full-size Fine-mesh Bundle Test (BFBT) benchmark data [6]. The BFBT benchmark provides unique high-resolution void fraction measurements for a wide variety of flow conditions and void fraction values, and allows assessing the accuracy of thermal-hydraulic models for two-phase flows in BWR geometries. We provide a recent view at best practices for CFD simulation of BWR fuel assemblies that can provide a useful reference to identify and overcome common challenges in the application of multiphase CFD tools.

2. BASELINE TWO-PHASE FLOW MODEL

2.1. Transport Equations

Eulerian-Eulerian multiphase approach with a baseline 'Zero Closure' has been implemented in the commercial CFD software, *STAR-CCM+ v11.04.010-R8*. The two-field formulation is employed as the M-CFD framework. Detailed descriptions of governing equations can be found in [**Error! Reference source not found.**] and [**Error! Reference source not found.**].

Mass conservation:

$$\frac{\partial}{\partial t}\int_V \alpha_i \rho_i \chi \, dV + \oint_A \alpha_i \rho_i \chi \left(\mathbf{v}_i - \mathbf{v}_g\right)\cdot d\mathbf{a} = \int_V \sum_{j\neq i}\left(\dot{m}_{ij} - \dot{m}_{ji}\right)\chi \, dV + \int_V S_i^{\alpha} dV \tag{1}$$

$$\sum_i \alpha_i = 1 \tag{2}$$

Momentum conservation:

$$\begin{aligned}&\frac{\partial}{\partial t}\int_V \alpha_i \rho_i \chi \mathbf{v}_i dV + \oint_A \alpha_i \rho_i \chi \mathbf{v}_i \otimes \left(\mathbf{v}_i - \mathbf{v}_g\right)\cdot d\mathbf{a} = -\int_V \alpha_i \chi \nabla p dV + \int_V \alpha_i \rho_i \chi \mathbf{g} dV \\ &+ \oint_A \left[\alpha_i\left(\tau_i + \tau_i^t\right)\right]\chi \cdot d\mathbf{a} + \int_V \mathbf{M}_i \chi \, dV + \int_V \left(\mathbf{F}_{\text{int}}\right)_i \chi \, dV + \int_V S_i^{v} \chi \, dV + \int_V \sum\left(\dot{m}_{ij}\mathbf{v}_j - \dot{m}_{ji}\mathbf{v}_i\right)\chi \, dV\end{aligned} \tag{3}$$

Energy conservation:

$$\begin{aligned}&\frac{\partial}{\partial t}\left(\alpha_i \rho_i E_i\right) + \nabla\cdot\left[\alpha_i \rho_i H_i\left(\mathbf{v}_i - \mathbf{v}_g\right)\right] + \nabla\cdot\alpha_i \mathbf{v}_g p = \nabla\cdot\left(\alpha_i k_{eff,i}\Delta T_i\right) + \nabla\cdot\left(\mathbf{T}_i\cdot\mathbf{v}_i\right) \\ &+ \mathbf{f}_i\mathbf{v}_i + \sum_{j\neq i} Q_{ij} + \sum_{(ij)} Q_i^{(ij)} + S_{u,i} + \sum_{j\neq i}\left(m_{ij} - m_{ji}\right)h_i\left(T_{ij}\right)\end{aligned} \tag{4}$$

In order to calculate the continuous and dispersed phase turbulence stresses used in Eqn. (3), the realizable k-ε turbulence model with high y+ wall treatment was employed. Details of Realizable k-ε

model implemented in *STAR-CCM+* software can be found in [**Error! Reference source not found.**]. Troshko-Hassan particle-induced turbulence model [8] is employed as source terms to account for the bubble-induced turbulence with model coefficient, C_3, of 0.45 and damping coefficient of 1.0. The source terms for turbulent kinematic energy and dissipation are given by Eqn. (5) and Eqn. (6), respectively, as follows:

$$S_{k_c} = \frac{3}{4}\frac{C_D}{D_b}\alpha_g \rho_l \left|\mathbf{v}_l - \mathbf{v}_g\right|^3 \tag{5}$$

$$S_{\varepsilon_c} = \frac{C_3 S_{k_c}}{t_b}. \tag{6}$$

2.2. A Baseline Zero Closure Model

The baseline Zero Closure model aims at a simple and robust representation of the key mechanisms of the physics of the two-phase flow, rather than aiming at the absolute accuracy of the predictions, as a consequence of the still limited high grade CFD experiments available to improve and validate the separate mechanisms. This paper reviews the details of Zero Closure model.

2.2.1. Interfacial area density and interaction length scale

Based on the surface area of spherical particle, the interfacial area density is modeled through the use of a Sauter mean diameter d_s [11] as follows:

$$a_{ij} = 6\alpha_g / d_s . \tag{7}$$

The Sauter diameter adopts and algebraic formulation to describe the interfacial variation among different flow regimes. The Sauter mean diameter of Zero Closure model given by Eqn. (8) is implemented in *STAR-CCM+* by means of user-defined function.

$$d_s = \begin{cases} 10.06\left(p/p_0\right)^{-0.098}\sqrt{\sigma/\Delta\rho g}\left[\min\left(\alpha_g, 0.118\right)\right]^{0.35} & \alpha_g < 0.4 \\ 1.9425\times10^{-3}\exp\left(2.3637\alpha_g\right) & 0.4 < \alpha_g < 0.8 \\ 0.864 D_h & 0.8 < \alpha_g \end{cases} \tag{8}$$

The Yoneda correlation [12] is used for the bubbly flow regime, when α_g<0.4. An exponential trend is chosen for the intermediate flow regimes (0.4≤α_g<0.8), while the channel hydraulic diameter D_h is used as the characteristic length scale in the annular flow region (α_g≥0.8) and has a numerical constant value of 0.01278 for this application. The constant is computed as the difference between the hydraulic diameter of the sub-channel of the fuel assembly and two times the film thickness, assumed as 1.0 mm.

2.2.2. Wall heat partitioning model

In order to represent the heat transfer between the heated wall and the fluid and the boiling at the wall, a previously validate form of the classic Kurul-Podowski mechanistic heat partitioning is applied [13]. The wall heat flux consists of three components as follows:

$$\dot{q}''_w = \left(\dot{q}''_{conv} + \dot{q}''_{evap} + \dot{q}''_{quench}\right)\left(1 - K_{dry}\right) + K_{dry}\dot{q}''_{dry}. \tag{9}$$

For liquid contact with the wall, the convective heat flux is given by:

$$\dot{q}''_{conv} = \frac{\rho_l c_{pl} u_l^*}{t_l^+}\left(T_w - T_l\right). \tag{10}$$

For vapor contact with the wall, the convective heat flux is given by:

$$\dot{q}''_{dry} = \frac{\rho_g c_{pg} u_g^*}{t_g^+}\left(T_w - T_g\right) \tag{11}$$

The wall contact area fraction is given by:

$$K_{dry} = \begin{cases} 0 & \alpha_\delta \le \alpha_{dry} \\ \beta^2(3-2\beta) & \alpha_{dry} < \alpha_\delta \end{cases} \tag{12}$$

where α_δ is the vapor volume fraction averaged over the bubbly layer thickness and α_{dry} is the wall dryout break-point with default value of 0.9. "Wall Cell" option for specifying the bubble layer thickness for the dryout criterion was employed.

The evaporative heat flux is determined as follows:

$$\dot{q}''_e = n'' f\left(\frac{\pi d_w^3}{6}\right)\rho_g h_{lg}. \tag{13}$$

In the Zero Closure, Lemmert-Chawla model [14, 15] for nucleation site number density given by Eqn.(14), Cole model [16] for bubble departure frequency given by Eqn. (15) and Tolubinsky-Kostanchuk model [17] for bubble departure diameter given by Eqn.(16) were employed to calculate the evaporative heat flux.

Lemmert-Chawla nucleation site number density is given by:

$$n'' = \left(m\Delta T_{\sup}\right)^p \tag{14}$$

where m=185.0 (1/K), p=1.805 and ΔT_{sup} is the wall superheat.

Cole bubble departure frequency is given by:

$$f = \sqrt{\frac{4}{3}\frac{g(\rho_l - \rho_g)}{d_w \rho_l}}. \tag{15}$$

Tolubinsky-Kostanchuk bubble departure diameter is given by:

$$d_w = d_0 \exp\left[-\frac{\Delta T_{sub}}{\Delta T_0}\right] \tag{16}$$

where d_0 is the reference diameter with default value of 0.6 mm, ΔT_0 is the reference subcooling with default value of 45 K and ΔT_{sub} is the subcooling of the liquid. The minimum and maximum values of bubble departure diameter were specified by 0.025 mm and 1.4 mm, respectively.

The quenching heat flux is obtained by Eqn. (17) using the Del Valle Kenning model [18] for bubble induced quenching heat transfer coefficient given by Eqn. (18).

$$\dot{q}''_{quench} = h_{quench}\left(T_w - T_{quench}\right) \tag{17}$$

The quenching heat transfer coefficient is determined by the Del Valle Kenning model as follows:

$$h_{quench} = 2K_{quench} f \sqrt{\frac{\rho_l c_{pl} k_l t_w}{\pi}} \tag{18}$$

where K_{quench} is the bubble influence wall area fraction, f is the bubble departure frequency, t_w is the waiting time between the bubble departure and the nucleation of the next bubble with wait coefficient of 0.8.

The bubble influence wall area fraction is obtained using Kurul-Podowski model [19] as follows:

$$K_{quench} = C_A \frac{\pi d_w^2}{4} n'' \tag{19}$$

where C_A is the area coefficient for scaling between the nucleation site area density and the wall area fraction the bubble-induced quenching influences with the default value of 2.0.

2.2.3. Interphase momentum transfer models

The interphase momentum transfer term, $\mathbf{M}_i$, represents the sum of all the liquid-vapor interfacial forces. The interphase momentum transfer term includes contributions from the drag, virtual mass, lift, turbulent dispersion and wall lubrication forces as follows:

$$\mathbf{M}_i = F_D + F_{VM} + F_L + F_{TD} + F_{WL} \tag{20}$$

where F_D is the drag force term, F_{VM} is the virtual mass force term, F_L is the lift force term, F_{TD} is the turbulent dispersion force term and F_{WL} is the wall lubrication force term.

The drag force term acting on the vapor phase due to the liquid phase is given in Eqn. (21). Tomiyama correlation [20] for a drag coefficient and the volume fraction exponent drag correction were used to calculate the drag force. Details of volume fraction exponent drag correction can be found in [**Error! Reference source not found.**].

$$F_D = f_D C_D \frac{1}{2} \rho_l \left(\mathbf{v}_l - \mathbf{v}_g\right) \left|\mathbf{v}_l - \mathbf{v}_g\right| \left(a_{ij}/4\right) \tag{21}$$

The virtual mass force is given by Eqn. (22) with a spherical particle virtual mass coefficient, C_{VM}, of 0.5.

$$F_{VM} = C_{VM}\rho_l\alpha_g\left(\frac{D\bar{u}_l}{Dt} - \frac{D\bar{u}_g}{Dt}\right) \tag{22}$$

The lift force term is given by Eqn. (23). While accurate lift closure are being developed, current work as evidenced the inapplicability of existing correlations [21]. The lift closure is leveraged to reproduce the key physical effect of bubble migration through a simple step function for lift coefficient given by Eqn. (24). A positive and constant value of 0.025 is used for α_g<0.25, representing almost spherical bubbles in the low void fraction regime, which accumulate near the wall; while a negative constant value of -0.025 for $\alpha_g \geq 0.25$, representing larger wobbly bubbles that migrate towards the center of the channel.

$$F_L = C_L\rho_l\alpha_g\left(\mathbf{v}_r \times \left(\nabla \times \mathbf{v}_l\right)\right) \tag{23}$$

$$C_L = \begin{cases} 0.025 & \alpha_g \leq 0.25 \\ -0.025 & 0.25 < \alpha_g \end{cases} \tag{24}$$

The turbulent dispersion force term is given by Eqn. (25) in a logarithmic form.

$$F_{TD} = A_D\frac{\nu_l^t}{\sigma_\alpha}\left(\nabla\ln(\alpha_l) - \nabla\ln(\alpha_g)\right) \tag{25}$$

where A_D is the mean linearized drag coefficient evaluated using a mean slip velocity and mean interfacial area, ν_c^t is the liquid phase turbulent kinematic viscosity and σ_α is the turbulent dispersion Prandtl number which was set to 1.0.

The wall lubrication force model given in Eqn. (26) is proposed by Antal et al. [22]. In Zero closure model, this wall lubrication formulation is employed with the calibration coefficients C_{w1} of -0.01 and C_{w2} of 0.05.

$$F_{WL} = -\alpha_g\rho_l\frac{\left|\mathbf{v}_g - \mathbf{v}_l\right|^2}{D_b}\max\left\{\left(C_{w1} + C_{w2}\frac{D_b}{y_w}\right), 0\right\}\mathbf{n} \tag{26}$$

2.2.4. Interphase mass transfer model

A correlation for the Nusselt number for each phase at the interface is required to model bulk boiling and condensation. Since the difference in temperature between the interface and the vapor phase is not significant, a constant value of Nusselt number for vapor phase was specified as 2.0, while Chen-Mayinger model [23] given by Eqn. (27) is employed to determine the continuous phase Nusselt number.

$$Nu_l = 0.185\mathrm{Re}_g^{0.7}\ \mathrm{Pr}_l^{0.5} \tag{27}$$

3. CFD MODELING OF THE NUPEC BFBT BENCHMARK

The M-CFD modeling capabilities and practicability for BWR fuel assembly were assessed against three steady-state test cases (4101-55, 4101-58 and 4101-61) of the NUPEC BFBT benchmark. The benchmark program selected these cases as validation problems for two-phase CFD modeling [7]. In these specific cases, the fuel assembly Type-4 with Ferrule-type spacers was used. Details of Ferrule-type spacer geometry can be found in [6]. The fuel bundle consists of 60 electrically-heated rods arranged in an 8×8

array, a water rod at the center of the assembly and 7 Ferrule-type spacer grids. The fuel assembly has a heated length of 3.708 m with a uniform axial power shape. The outer diameter of heater rod and rod pitch are 12.3 mm and 16.2 mm, respectively. The diameter of water rod is 34.0 mm. The inner width of channel box is 132 mm, and the corner radius of channel box is 8.0 mm. The channel flow area is 9,463 mm^2. The thicknesses of inner rings and outer rim of spacer are 0.5 mm and 1.0 mm, respectively. The height of spacer is 31.0 mm.

3.1. Geometric Modeling of BFBT Fuel Assembly

Figure 1 shows the geometrical configuration of the CFD model for the BFBT fuel bundle. The fuel assembly geometry has been simplified by removing dimples and springs from the original spacer geometry. Mixing tabs on the outer rim of spacer have also been removed from the model geometry Since the Ferrule-type spacer consists of inner annuli that are in contact with each other, a line contact would exists at these locations, which is not representative of a production spacer, and would introduce challenges in the mesh discretization. In order to prevent poor quality mesh in the contact region this was modified, as shown in Fig. 1, by introducing a larger contact area. The flow area variation due to these modifications is less than 0.1 %.

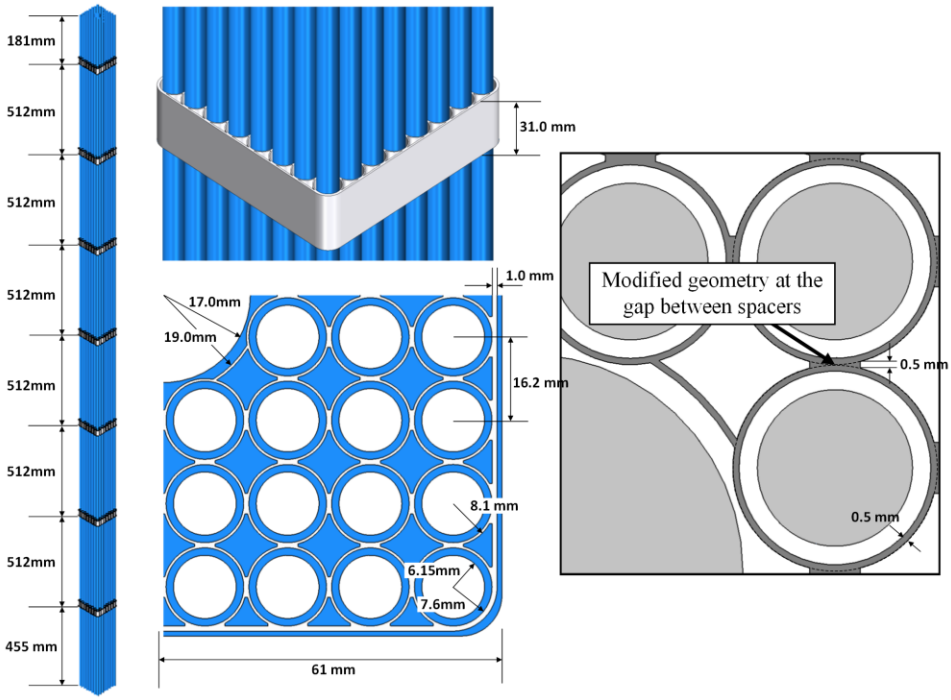

Figure 1. Computational domain of BFBT fuel bundle Type-4 with spacer grids

Figure 2 shows the mesh structure of CFD model. A hexa-dominant trimmed mesh, in combination with boundary fitted prism layers was generated with the built-in mesh generation capabilities of *STAR-CCM+* software. The mesh adopted is relatively coarse, and was selected from separate sensitivity studies. A uniform cell size of 2.0 mm is used away from the wall, while the prism boundary layer total thickness was specified to be 0.5 mm, and two layers are implemented to guarantee a $y+$ value for the near wall cell between 30 and 100. The total number of cells is 11.42 million. In this work, cell sizes less than 2.0 mm were also tested but resulted in the generation of a few low quality cells in the contact areas that created convergence issues. Further work is required in the future to address this problem in generating finer computational meshes. Figure 3 shows the cell quality metrics on two cross-sectional planes at different elevations. This cell quality metrics is based on a hybrid of the Gauss and least-squares methods for cell

gradient calculation methods, which allows accounting for both the relative geometric distribution of the cell centroids of the neighbor cells, and the orientation of the cell faces. Flat cells with highly non-orthogonal faces have a low cell quality, and in two-phase flow boiling simulation have a significant influence on the stability and robustness of the simulation. Poor quality mesh in current M-CFD solvers can lead to strong local temperature over- and under-shoot and most often results in code instability. Point and line contacts in the fuel spacer region are the most common areas leading to poor quality mesh and special care should be taken to avoid having these types of geometric features. Replacing point contact or line contact in geometry with an approximated surface contact is often sufficient to improve mesh quality. The minimum mesh quality of this model was approximately 0.1 and the volume-averaged mesh quality of computational domains were 0.955.

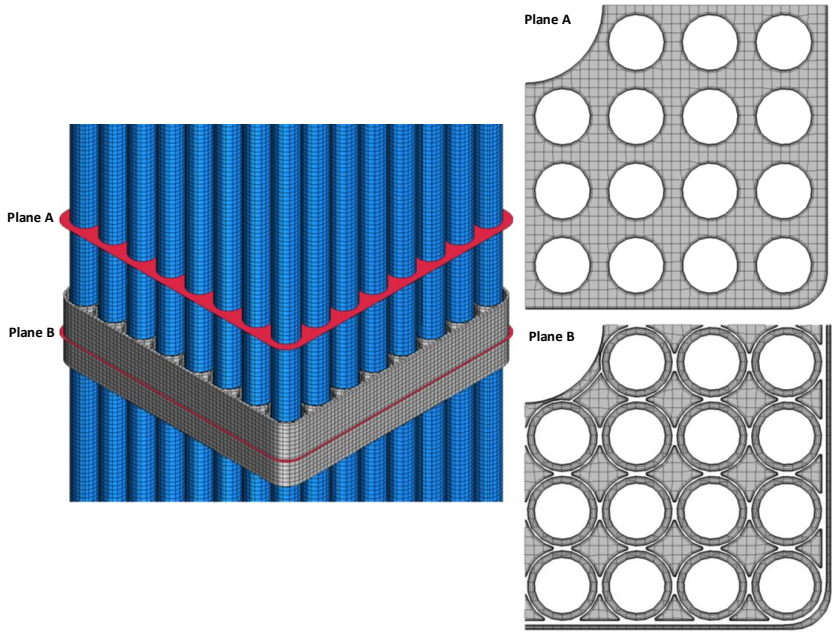

Figure 2. Mesh structure of CFD model

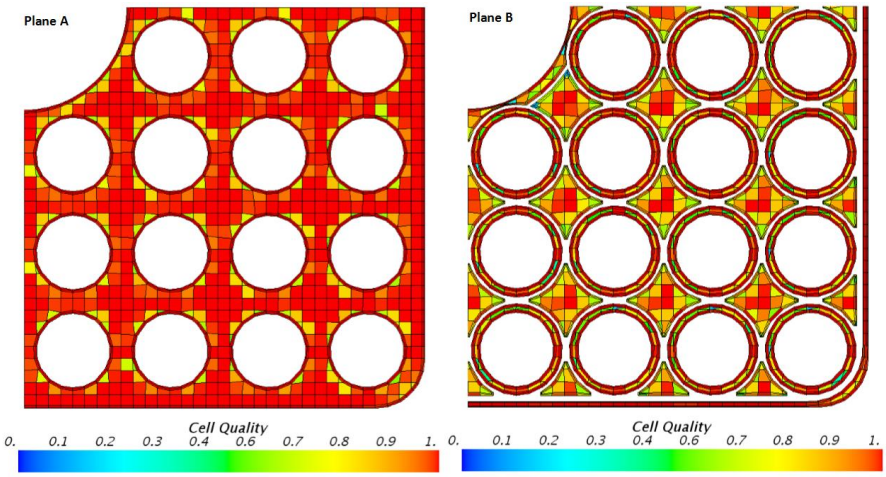

Figure 3. Mesh qualities on the cross-sectional planes of the CFD model

3.2. Initial and Boundary Conditions

The characteristic radial power distribution inside a fuel assembly is reproduced imposing a different heat flux, through a different multiplier, to the heating rods, as shown in Fig. 4. The operating conditions of three test cases were tabulated in Table I. Inlet liquid and vapor temperatures were specified as 551.096 K and 560.538K, respectively, and the operating pressure was set to approximately 7.2 MPa. The mass flow rate of the tests was 15.28 kg/s. The inlet velocity profile, turbulent kinetic energy and turbulent dissipation rate were specified to the inlet boundary as obtained from a separate fully developed single-phase flow simulation of the fuel bundle. The volume fractions of liquid and vapor at the inlet boundary were set to 0.999 and 0.001, respectively. Flow-split outlet boundary condition was specified to the outlet boundary with a split ratio of 1.0.

A (for Assembly 4, C2A, C3)

1.15	1.30	1.15	1.30	1.30	1.15	1.30	1.15
1.30	0.45	0.89	0.89	0.89	0.45	1.15	1.30
1.15	0.89	0.89	0.89	0.89	0.89	0.45	1.15
1.30	0.89	0.89			0.89	0.89	1.15
1.30	0.89	0.89			0.89	0.89	1.15
1.15	0.45	0.89	0.89	0.89	0.89	0.45	1.15
1.30	1.15	0.45	0.89	0.89	0.45	1.15	1.30
1.15	1.30	1.15	1.15	1.15	1.15	1.30	1.15

Figure 4. Radial power shape of test assembly type-4 [7]

Table I. Test conditions for steady-state BFBT test cases [7]

Test No.	Pressure (MPa)	Flow rate (t/h)	Inlet sub-cooling (kJ/kg)	Power (MW)	Exit Quality (%)
4101-55	7.195	54.59	52.9	1.92	5
4101-58	7.152	54.58	50.6	3.52	12
4101-61	7.180	54.65	52.5	6.48	25

3.3. Configurations of Solver Parameters

The solver Under-Relaxation Factors (URFs) required for Eulerian multiphase flow simulations are smaller than those for single-phase simulation. According to recommended best practices by S. Lo [24], the URFs of 0.1 for pressure and volume fraction, 0.3 for velocity, turbulence and temperature and 0.5 for other variables are recommended values for code convergence. In this study, the implicit and explicit URFs for phase coupled velocity and volume fraction were set to 0.9 and 0.1, respectively. So, the overall URFs for phase coupled velocity and volume fraction were specified to be 0.09. The URF for pressure was set to 0.1 and for other variables were set to 0.5. 2^{nd}-order convection scheme for velocity and 1^{st}-order convection scheme for volume fraction were employed with minimum volume fraction of zero. In this work, convergence was not reached when higher values of URFs were specified. The number of iterations required for convergence increases with lowering the values of the specified URFs. Thus, it is recommended to not use values of URFs that are excessively small.

4. RESULTS AND DISCUSSION

The M-CFD simulations have been carried out with the commercially available CFD software, *STAR-CCM+ v11.04.010-R8*, on one of the Idaho National Laboratory (INL) High Performance Computing

(HPC) clusters, the *Falcon*. The *Falcon* is the INL's flagship cluster with 600 TFlops of performance and 121 TB total memories. Parallel computations using 500 processes for 3,000 iterations took less than 2 hours of execution time. In order to quantitatively assess the accuracy of the Zero Closure, local void fraction profiles, sub-channel averaged void fraction and exit quality are analyzed. Figure 5 shows the lines and the sub-channel locations on the outlet boundary surface for the comparison of CFD results against experimental data. Figures 6−8 show the profiles of normalized void fraction as a function of relative distance from the center of rod bundle along different lines. The local void fraction was normalized based on the mean void fraction on each line. The Zero Closure predicts the local void fraction profiles well. CFD results and experiments are in good agreement. The void fractions in bulk regions of subchannel tend to be relatively higher than that in the narrow region between the heater rods. These patterns indicate as expected that the bubbles lifted off from the heated surface cluster in the bulk region of the flow. For case BFBT-4101-61 case, the local variation of void fraction distribution is relatively smaller than in the other cases. As the overall void fraction decreases, the deviation of void fraction between near-wall region and bulk region increases. In those cases with lower void fraction conditions, the interfacial forces of Zero Closure, such as lift force, wall lubrication force, etc., would overestimate their impacts.

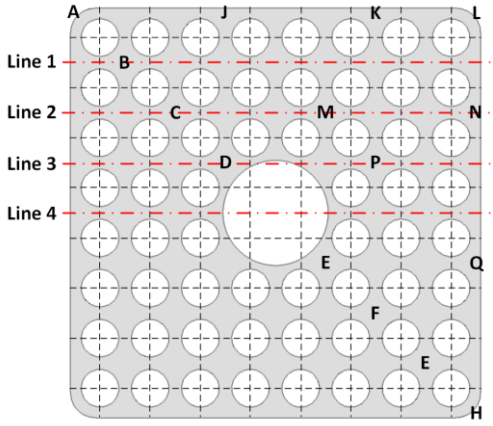

Figure 5. Reference sub-channels location

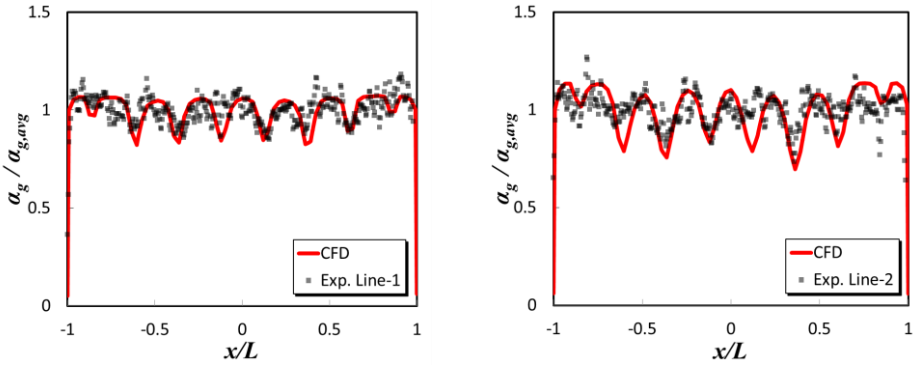

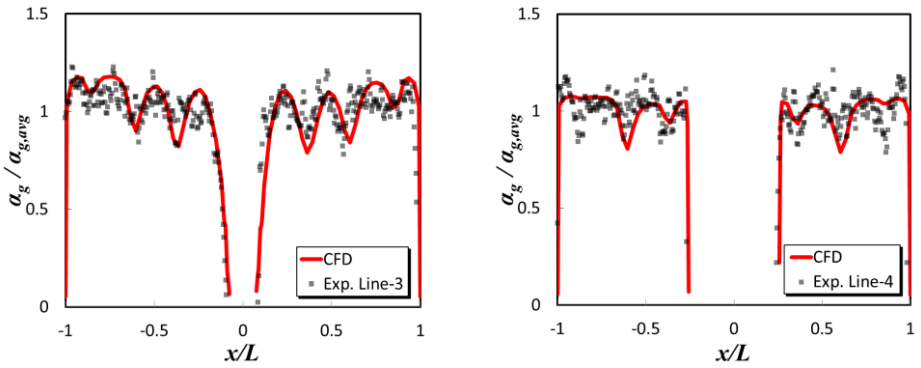

Figure 6. Normalized local void fraction profiles (BFBT 4101-61)

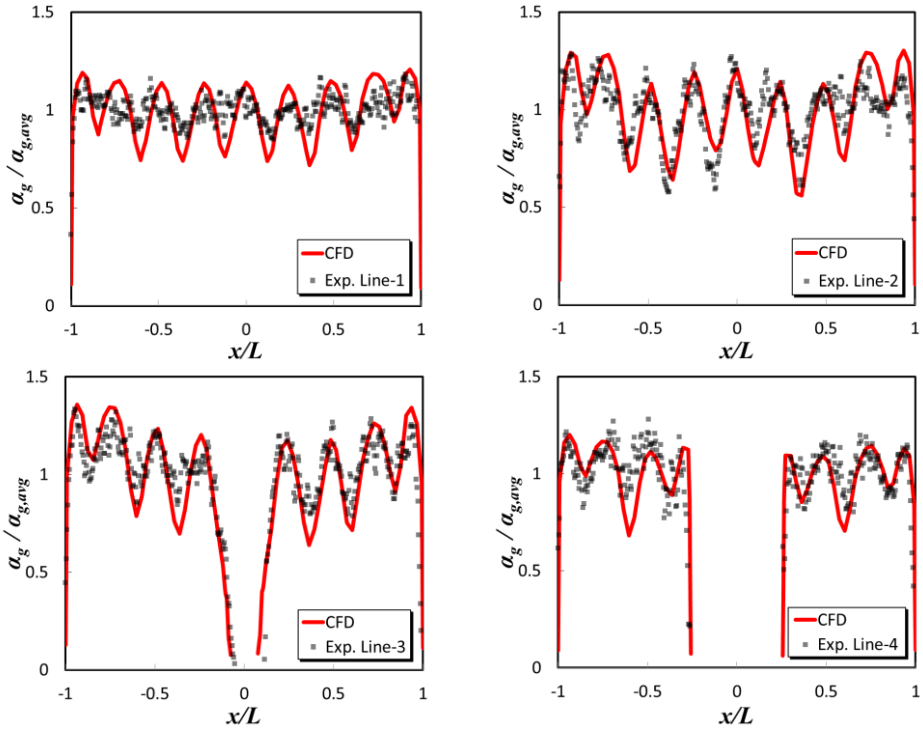

Figure 7. Normalized local void fraction profiles (BFBT 4101-58)

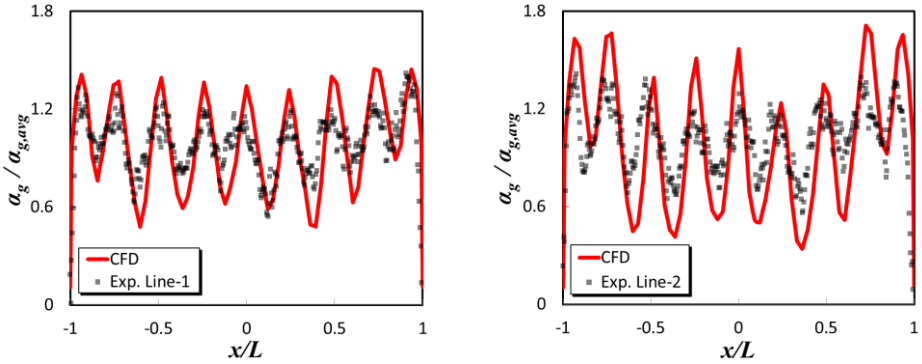

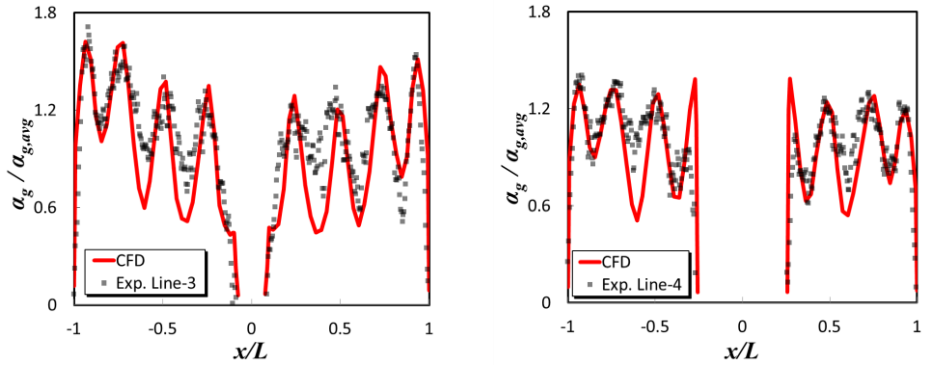

Figure 8. Normalized local void fraction profiles (BFBT 4101-55)

Figure 9 shows the computed normalized void fraction as a function of experimental void fraction. CFD results and experiments agree within a deviation of ± 20% at higher void fraction conditions (BFBT-4101-61). In this case, some data points are further away from the error boundaries and correspond to the regions near the wall. The deviation increases in the cases with lower void fraction conditions. For the BFBT-4101-58 case, it increases up to ± 30% while the BFBT-4101-55 case shows a relatively larger deviation, ranging between -50% and +35%. Results evidence that the M-CFD with Zero Closure shows impressive applicability to high void fraction conditions, while accurate prediction of lower void fraction conditions will require improvement of the hydrodynamic closures for transversal forces, lift and turbulent dispersion, particularly in the transition region between wall peaked and bulk picked void distributions.

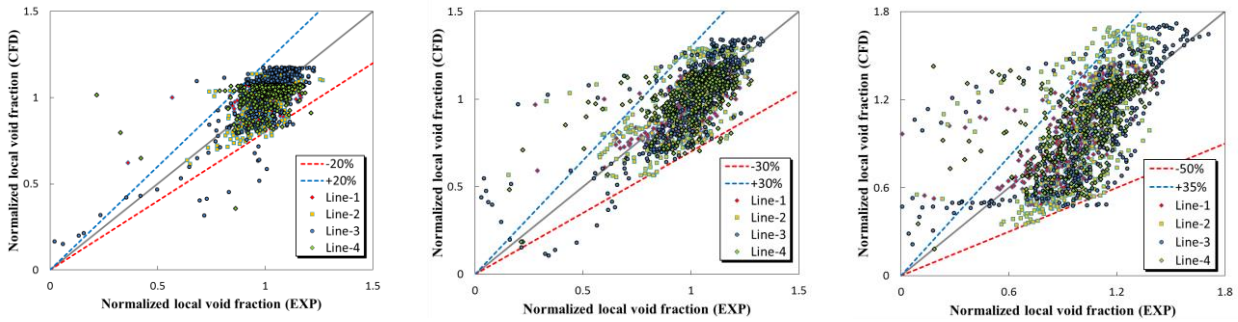

(a) BFBT-4101-61 (b) BFBT-4101-58 (c) BFBT-4101-55

Figure 9. Comparisons of experimental and computational normalized void fractions

Figure 10 shows sub-channel averaged void fraction errors. These were obtained by averaging the computed local void fractions in each subchannel. The error was calculated by subtracting the experimental sub- averaged value from the computed void fractions. In most of the sub-channels, the averaged void fraction error is less than ±10%, with a few outliers where the error remains below ±18%.
The computational average void fractions of BFBT-4101-61, 4101-58 and 4101-55 were 80.77%, 62.99% and 43.79%, respectively. The corresponding experimental results were 80.64%, 63.18% and 42.75%, respectively. Computational exit qualities of BFBT-4101-61, 4101-58 and 4101-55 were 24.49%, 11.91% and 4.92%, respectively. The computational exit qualities well agree with experimental data (25%, 12% and 5%) within the relative deviation of 2%.

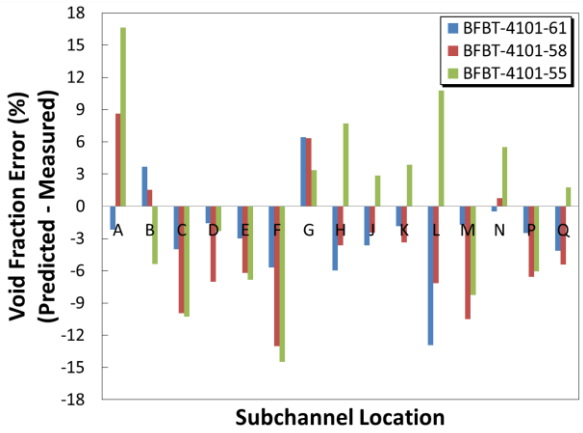

Figure 10. Subchannel void fraction error for selected subchannels

5. CONCLUSIONS

In this work, a Zero closure model has been implemented in the commercially available *STAR-CCM+ v11.01-010-R8* CFD software, for application to BWR fuel assembly simulation. The capabilities of M-CFD for various void fraction regimes, particularly focusing on high void fraction conditions, were assessed against the international OECD/NRC BFBT benchmark data. Although simple approaches were employed for this Zero Closure, the CFD simulation results are in impressive agreement with experimental data in terms of local void fraction profile, subchannel void fraction and exit quality. Comparison against lower void fraction conditions results show the need for further improvement of the closure in this regime, where the lift and turbulent dispersion forces do not appropriately capture the transition between wall-peaked and bulk-peaked distributions. As current Best Practices of M-CFD for BWRs, it is recommended to: (1) simplify the spacer geometry in order to prevent poor cell quality in the spacer grids area; (2) adopt a relatively large cell size around 2.0 mm, avoiding low quality cells at the contact points, with boundary fitted prism layer leading to appropriately high y+ value; (3) choose appropriate solver under-relaxation factors in order to assist the convergence of simulation; (4) utilize massively parallel computation for computational costs reduction and simulation feasibility.

NOMENCLATURE

A_D	Mean linearized drag coefficient	S_{k_c}	Turbulent kinematic energy source term
a_{ij}	Interfacial area density	S_{ε_c}	Turbulent dissipation source term
C_D	Drag Coefficient	S_i^{α}	Phase mass source term
c_p	Specific heat	S_i^{v}	Phase momentum source term
D_b	Bubble diameter	$S_{u,i}$	Energy source term
d_w	Bubble departure diameter	T	Temperature
E	Total energy	$\mathbf{T}_i$	Viscous stress tensor
F	Interfacial forces	t_w	Waiting time
f	Bubble departure frequency	$\mathbf{v}$	Velocity vector
f_D	Drag correction factor	y_w	Distance from the wall to the bubble
$\mathbf{F}_{int}$	Internal forces	α	Volume fraction
$\mathbf{f}$	Body force vector	α_{dry}	Wall dryout break-point
$\mathbf{g}$	Gravity vector	ν_c^t	Liquid phase turbulent kinematic viscosity
H	Total enthalpy	ρ	Density

$h_i(T_{ij})$	Phase i enthalpy at interface temperature T_{ij}	σ_α	Turbulent dispersion Prandtl number
h_{lg}	Latent heat of fluid	τ_i	Molecular stress
h	Heat transfer coefficient	τ_i^t	Turbulent stresses
k	Thermal conductivity	χ	Void fraction
K_{dry}	Wall dryout area fraction		
K_{quench}	Quenching influence wall area fraction	***Subscripts***	
$\mathbf{M}_i$	Interphase momentum transfer	D	Drag force
$\dot{m}_{ij}$	Mass transfer rate to phase i from phase j	eff	Effective
$\dot{m}_{ji}$	Mass transfer rate to phase j from phase i	g	Vapor phase
n''	Nucleation site density	L	Lift force
p	Pressure	l	Liquid phase
Q	Interphase heat transfer rate	$quench$	Quenching
$\dot{q}''_{conv}$	Convective heat flux	TD	Turbulent dispersion force
$\dot{q}''_{dry}$	Vapor contribution to convective heat flux	VM	Virtual mass force
$\dot{q}''_{evap}$	Evaporative heat flux at wall	w	Wall
$\dot{q}''_{quench}$	Quenching heat flux	WL	Wall lubrication force

ACKNOWLEDGMENTS

This work was supported by the Consortium for Advanced Simulation of Light Water Reactor, an Energy Innovation Hub for Modeling and Simulation of Nuclear Reactors under U.S. Department of Energy Contract No. DE-AC05-00OR22725.

REFERENCES

1. A. Tentner, S. Lo, A. Ioilev, M. Samigulin and V. Ustinenko, "Computational Fluid Dynamics Modeling of Two-phase Flow in a Boiling Water Reactor Fuel Assembly," *Mathematics and Computation, Supercomputing, Reactor Physics and Nuclear and Biological Applications*, Avignon, France, Sept. 12-15 (2005).
2. A. Tentner, S. Lo, A. Ioilev, M. Samigulin, V. Ustinenko and V. Kozlov, "Advances in Computational Fluid Dynamics Modeling of Two-phase Flow in a Boiling Water Reactor Fuel Assembly," *Proceedings of the 14th International Conference on Nuclear Engineering ICONE14*, Miami, FL, July 17-20, (2006).
3. A. Tentner, S. Lo, A. Ioilev, V. Melnikov, M. Samigulin, V. Ustinenko, and S. Melinikova, "Computational fluid dynamics modeling of two-phase flow topologies in a Boiling Water Reactor fuel assembly," *Proceedings of the 16th International Conference on Nuclear Engineering ICONE16*, Orlando, Florida, May 11-15 (2008)
4. V. Ustinenko, M. Samigulin, A. Ioilev, S. Lo, A. Tentner, A. Lychagin, A. Razin, V. Girin and Ye. Vanyukov, "Validation of CFD-BWR, a New Two-phase Computational Fluid Dynamics Model for Boiling Water Reactor Analysis," *Nuclear Engineering and Design*, **238**, pp.660-670 (2008).
5. A. Tentner, W.D. Pointer, S. Lo and A. Splawski, "Development and Validation of a Computational Fluid Dynamics Model for the Simulation of Two-phase Flow Phenomena in a Boiling Water Reactor Fuel Assembly," *Proceedings of the 17th International Conference on Nuclear Engineering ICONE18*, Brussels, Belgium, July 12-16, (2009).
6. W.K. In, D.H. Hwang and J.J. Jeong, "A Subchannel and CFD Analysis of Void Distribution for the BWR Fuel Bundle Test Benchmark," *Nuclear Engineering and Design*, **258**, pp. 211-225 (2013).
7. B. Neykov, F. Aydogan, L. Hochreiter, K. Ivanov, H. Utsuno, K. Kasahara, E. Sartori and M. Martin, "Nupec BWR Full-size Fine-mesh Bundle Test (BFBT) Benchmark, Volume I: Specification," OECD, Nuclear Energy Agency, NEA no. 6212, ISBN 92-64-01088-2 (2006).
8. G. H. Yeoh and J. Tu, Computational Techniques for Multiphase Flows, Butterworth Heinemann, 2009.
9. Siemens PLM Software Inc., STAR-CCM+ v11.04 User Guide, (2016).
10. A.A. Troshko, and Y.A. Hassan, "A two-equation turbulence model of turbulent bubbly flows", *International Journal of Multiphase Flow*, **27**, pp. 1965-2000 (2001).
11. M. Ishii and T. Hibiki, *Thermo-Fluid Dynamics of Two-Phase Flow*, Springer, New York, USA (2006).
12. K. Yoneda, A. Yasuo and T. Okawa, "Flow structure and bubble characteristics of steam-water two-phase flow in a large-diameter pipe," *Nuclear Engineering and Design*, **217**, pp. 267-281 (2002).
13. E. Baglietto and M.A. Christon, "Demonstration & Assessment of Advanced Modeling Capabilities for Multiphase Flow with Sub-cooled Boiling", CASL Technical Report: CASL-U-2013-0181-001 (2013).
14. M. Lemmert, and J.M. Chawla, "Influence of flow velocity on surface boiling heat transfer coefficient," *Heat Transfer in Boiling*, pp. 237-247 (1977).
15. M.Z. Podowski, and R.M. Podowski, "Mechanistic Multidimensional Modeling of Forced Convection Boiling Heat Transfer", *Science and Technology of Nuclear Installations*, Article ID 387020, 10 pages (2009).
16. R. Cole, "A photographic study of pool boiling in the region of the critical heat flux", *AIChE J.*, **6**, pp. 533-542 (1960).

17. V.I. Tolubinsky and D.M. Kostanchuk, “Vapour bubbles growth rate and heat transfer intensity at subcooled water boiling”, *Heat Transfer* 1970, *Preprints of papers presented at the 4th International Heat Transfer Conference*, Paris, **5**, Paper No. B-2.8, (1970).
18. M.V.H. Del Valle and D.B.R. Kenning, “Subcooled flow boiling at high heat flux”, *Int. J. Heat Mass Transfer*, **28**, pp. 1907-1920 (1985).
19. N. Kurul, and M.Z. Podowski, “Multidimensional effects in sub-cooled boiling”, *Proceedings of the 9th Heat Transfer Conference*, Jerusalem, Israel, Aug. 19-24 (1990).
20. A. Tomiyama, I. Kataoka, I. Zun and T. Sakaguchi, “Drag Coefficients of single bubbles under normal and micro gravity conditions”, *JSME International Journal*, Series B, **41**(2), pp. 472-479 (1998).
21. R. Surgue and E. Baglietto, “A reevaluation of the lift force in Eulerian multiphase CFD,” *The 16th International Topical Meeting on Nuclear Reactor Thermal Hydraulics NURETH-16*, Chicago, Illinois, Aug.30−Sept.4 (2015).
22. S.P. Antal, R.T. Lahey and J.E. Flaherty, “Analysis of phase distribution in fully developed laminar bubbly two-phase flow”, *Int. J. Multiphase Flow*, **17**, pp. 635–652 (1991).
23. Y.M. Chen and F. Mayinger, “Measurement of heat Transfer at Phase Interface of Condensing Bubble,” *Int. J. Multiphase Flow*, **18**, pp. 877-890 (1992).
24. S. Lo, “What are the Recommended Best Practices while Troubleshooting an Eulerian Multiphase Simulation?” https://steve.cd-adapco.com/articles/en_US/FAQ/SL-5-092?type=pdf, Article number: 3519 (2015).